

Analysis of luminosity measurements of the pre-white dwarf PG 1159-035

E. Matsinos*

*Electronic mail: evangelos (dot) matsinos (at) sunrise (dot) ch

Abstract

The study of the luminosity measurements of the pre-white dwarf PG 1159-035 has established the properties of the rich power spectrum of the detected radiation and, derived thereof, the physical properties of this celestial body. Those of the measurements which are available online are analysed in this work from a different perspective. After the measurements were band-passed, they were split into two parts (of comparable sizes), one yielding the training (learning) set (i.e., the database of embedding vectors and associated predictions), the other the test set. The optimal embedding dimension $m_0 = 10$ was obtained using Cao's method; this result was confirmed by an analysis of the correlation dimension. Subsequently, the extraction of the maximal Lyapunov exponent λ was pursued for embedding dimensions m between 3 and 12; results were obtained after removing the prominent undulations of the out-of-sample prediction-error arrays $S(k)$ by fitting a monotonic function to the data. The grand mean of the values, obtained for sufficient embedding dimensions ($10 \leq m \leq 12$), was: $\lambda = (9.2 \pm 1.0(\text{stat.}) \pm 2.7(\text{syst.})) \cdot 10^{-2} \Delta\tau^{-1}$, where $\Delta\tau = 10$ s is the sampling interval in the measurements. On the basis of this significantly non-zero result, it may be concluded that the physical processes, underlying the variation of the luminosity of PG 1159-035, are non-linear. The aforementioned result for λ was obtained using the L^∞ -norm distance; a larger, yet not incompatible, result was extracted with the Euclidean (L^2 -norm) distance.

PACS 2010: 05.10.-a; 05.45.-a; 05.45.Gg; 45.30.+s; 95.10.Fh

Key words: Statistical Physics and Nonlinear Dynamics; Linear/Nonlinear Dynamical Systems; Applications of Chaos; Chaos Astronomy

1 Introduction

When the hydrogen reserves of a star are exhausted, the star collapses until the temperature in its core enables helium to ignite and burn to carbon. To determine the fate of the star, one only needs to know its mass. For stellar

masses comparable to the Solar mass (M_{\odot}), the outer shells of the star evaporate into space (planetary nebula) leaving a relic at the centre, which evolves into a white dwarf. Discovered in 1977 in a project aiming at the identification of ultraviolet-excess stellar sources (Palomar-Green survey) [1], PG 1159-035 is a celestial body in the Constellation of Virgo, which the experts in the domain of Stellar Evolution place in a transitional phase, from the central star of a planetary nebula to a white dwarf. PG 1159-035 contains about 60% of the solar mass, confined within a radius of about 2.5% of the solar radius (about 2.7 times the radius of the Earth), and is a few hundred times more luminous than our Sun. Stellar bodies in this transitional phase are known as ‘pre-white dwarves’.

The variation of the luminosity of the pre-white dwarf PG 1159-035, arising from non-radial gravity-wave (g -wave) pulsations, was measured (for the first time to that detail) by the Whole Earth Telescope (WET) in 1989. The members of the Collaboration introduce the WET project as “a global, interactive network of photometric observers who together provide essentially continuous coverage of a set of prioritised targets.” [2] The pre-white dwarf PG 1159-035 might have attracted original attention because its “near-equatorial declination allowed observatories in both hemispheres to participate in the observations.”

The analysis of the measurements, spanning over 229 effective hours (hr) of data acquisition, revealed 122 pulsation modes, with periods ranging from 300 to 1000 s [2]. Those of us who do not frequently come across Fourier transforms with a resolution of $1 \mu\text{Hz}$ will undoubtedly be impressed by Fig. 4 of Ref. [2]. That work set the region of interest in the power spectrum of the detected light (p. 330): “The peaks of greatest power in the Fourier spectrum are largely confined to the interval between 1000 and 2600 μHz , with the dominant power in the narrower interval between 1750 and 2250 μHz .” Reference [2] was also important for another, less obvious reason: it cemented the foundations of the domain of Asteroseismology, as the discipline studying the “stellar structure and evolution as revealed by global stellar oscillations.” To provide an idea of what may be learnt from the analysis of such observations, the authors of Ref. [2] write (about PG 1159-035) in the abstract of their paper: “We find its mass to be $0.586 M_{\odot}$, its rotation period 1.38 days, its magnetic field less than 6000 G, its pulsation and rotation axes to be aligned, and its outer layers to be compositionally stratified.”

The entirety of the luminosity measurements of PG 1159-035 (runs between 1979 and 2002) were analysed in a more recent paper [3], leading to the detection of 76 additional (i.e., on top of those which had been identified in Ref. [2]) pulsation modes. As the authors mention in the abstract of their paper, the $122 + 76 = 198$ known pulsation modes of PG 1159-035 represent “the largest number of modes detected in any star besides the Sun.” Furthermore, Ref. [3]

improved on the accuracy of the physical quantities of PG 1159-035, e.g., on its rotation period (1.3920 ± 0.0008 days), and provided updated estimates for the object's mass ($0.59 \pm 0.02 M_{\odot}$) and magnetic field (< 2000 G).

A number of models, aiming at the description of the measurements obtained from PG 1159-035 and from similar stars in terms of the physical processes in the interior of these bodies, may be found in the literature [4,5,6,7,8,9]. The free parameters of these models include the stellar mass, the effective temperature T_{eff} , the surface helium-layer thickness (usually expressed as a fraction of the stellar mass), and the stellar composition. Using such models, knowledge may be gained of the temporal evolution of celestial bodies which have split off from the so-called Post-Asymptotic Giant Branch, a horizontal branch in the Hertzsprung-Russell diagram, characterised by nearly constant luminosity and sharply decreasing temperature. The temporal evolution of these stars follows mass-dependent curves in the $(\lg T_{\text{eff}}, \lg g)$ plane¹, where g stands for the ratio of the gravitational acceleration at the surface of the star to that at the surface of the Earth.

By variation of the free parameters of the aforementioned models, stellar solutions are obtained and allowed to evolve in time. A database of stellar states (snapshots in the evolution of each simulated body) is thus created. After the (time-dependent) predictions for the pulsation spectra are obtained in each of these solutions, the database element, which best resembles the pulsation spectra obtained from the luminosity measurements of a given source, may be identified. Reliable information on the progenitor of the specific object, as well as forecasts for its future, may thus be obtained.

References [4,5,6,7,8,9] look at each such celestial body from the point of view of Physics, i.e., attempting its description in terms of the established principles of Astrophysics and, in particular, of Stellar Evolution. This work looks at the acquired data from a different perspective, investigating the possibility that the data alone could provide an answer on whether the physical processes, generating the observations, are linear or non-linear. Knowledge of the physical system is used as input only in the filtering of the scalar time-series measurements, namely in setting the appropriate band-pass/stop characteristics, as they have been known from Refs. [2,3]. To the best of my knowledge, this is the first study of the time-series measurements of PG 1159-035 from the perspective of non-linear dynamics.

This work uses those of the time-series measurements of PG 1159-035, which may be found (among other data from a variety of scientific domains) in the web site [10] (data set E); henceforth, these measurements will be referred to as 'original' (though, in reality, they have been selected from a larger set of

¹ Of course, $\lg x := \log_{10} x$.

data). Reference [10] does not provide information on how the available data has been obtained from the set of measurements acquired in the WET 1989 runs.

The software development, relating to this work, is part of a broader and more ambitious programme, aiming at robust analyses of time series via the application of user-selected linear and/or non-linear methods. Free software performing such analyses has been available since a long time, e.g., see Ref. [11].

2 The original time-series arrays

Seventeen data sets, containing luminosity measurements of PG 1159-035 from the 1989 runs, may be found in the web page [10]. These data sets carry the prefix ‘SF_E_’, which will be replaced here by ‘E’. The total number of measurements in these files is 27191, corresponding to an effective time of 271910 s. On the other hand, more measurements are shown² in Fig. 1 of Ref. [2]. Furthermore, from Table 1 of Ref. [3] one extracts the information that a total of 82471 measurements had been acquired in the 1989 runs, i.e., about three times the amount of measurements found in Ref. [10]. As a result, it is not easy to determine which parts of the data, acquired in the 1989 runs, found their way into the snippets of measurements contained in the database of Ref. [10]. Some statistical information on the seventeen time series of Ref. [10] is given in Table 1.

Difficulties with astronomical observations, in particular with those conducted via ground-based telescoping, are not infrequent; they may be caused by a variety of phenomena, predominantly atmospheric (turbulence, humidity, cloud coverage, etc.), but also relating to the position and the brightness of the Moon. Visual inspection of the luminosity measurements of PG 1159-035 reveals that, though an underlying oscillatory pattern in the intensity of the detected radiation is observed, a number of issues need to be resolved prior to the commencement of the data analysis. To start with, a large amount of noise seems to be present in the measurements. In this respect, the most extreme case appears to be the data set E05, shown in Fig. 1. In addition to the obvious ‘high-frequency’ noise, patterns in the data resemble those emanating from a drifting or oscillating calibration. There are cases in which a sizeable ‘drop of the values’ appears around the middle of the data set, as in files E02, E15, and E16. Transient effects are also seen, e.g., over the first 100 measurements

² In the caption of Fig. 1 of Ref. [2], it is mentioned that the data shown therein corresponds to the central 6 days of the run. Therefore, one might be led to conclude that the displayed data represent a fraction of the luminosity measurements collected in the WET project in the 1989 runs.

Table 1

Quantities relating to the available luminosity measurements of PG 1159-035, obtained from Ref. [10] (data set E therein). The columns correspond to an identifier of each time-series array, the number of its measurements (N), its minimal and maximal values (s_{\min} and s_{\max} , respectively), the range of variation of its entries, the average, and the root-mean-square (rms) of the signal in the data set. In the data acquisition, the sampling frequency was 100 mHz (hence the Nyquist frequency f_N was 50 mHz) and, naturally, the sampling interval $\Delta\tau$ was 10 s. For the sake of example, the data set E01 contains continuous luminosity measurements spanning about 1 hr and 42 minutes.

Data set	N	s_{\min}	s_{\max}	$s_{\max} - s_{\min}$	$\langle s \rangle$	rms
E01	617	-0.3153	0.2904	0.6057	$3.03 \cdot 10^{-4}$	$1.27 \cdot 10^{-1}$
E02	1255	-0.3053	0.3398	0.6451	$-4.65 \cdot 10^{-5}$	$1.03 \cdot 10^{-1}$
E03	1221	-0.2956	0.2713	0.5669	$1.02 \cdot 10^{-4}$	$9.49 \cdot 10^{-2}$
E04	979	-0.3290	0.3149	0.6439	$1.21 \cdot 10^{-4}$	$1.08 \cdot 10^{-1}$
E05	549	-0.3223	0.2991	0.6214	$-1.59 \cdot 10^{-4}$	$1.03 \cdot 10^{-1}$
E06	1553	-0.3163	0.3401	0.6564	$1.12 \cdot 10^{-4}$	$1.08 \cdot 10^{-1}$
E07	1936	-0.5947	0.6315	1.2262	$4.55 \cdot 10^{-5}$	$1.73 \cdot 10^{-1}$
E08	2495	-0.4549	0.3760	0.8309	$-7.09 \cdot 10^{-5}$	$1.45 \cdot 10^{-1}$
E09	1940	-0.6010	0.5801	1.1811	$5.78 \cdot 10^{-5}$	$1.57 \cdot 10^{-1}$
E10	1471	-0.4623	0.4568	0.9191	$6.43 \cdot 10^{-5}$	$1.48 \cdot 10^{-1}$
E11	2605	-0.5454	0.6033	1.1487	$1.19 \cdot 10^{-2}$	$1.82 \cdot 10^{-1}$
E12	1548	-0.5415	0.3590	0.9005	$6.36 \cdot 10^{-5}$	$1.28 \cdot 10^{-1}$
E13	2568	-0.3857	0.3906	0.7763	$-5.84 \cdot 10^{-7}$	$1.17 \cdot 10^{-1}$
E14	2602	-0.4517	0.4022	0.8539	$-1.65 \cdot 10^{-3}$	$1.32 \cdot 10^{-1}$
E15	672	-0.4322	0.6539	1.0861	$-3.38 \cdot 10^{-4}$	$1.79 \cdot 10^{-1}$
E16	1512	-0.5381	0.6366	1.1747	$5.22 \cdot 10^{-3}$	$1.84 \cdot 10^{-1}$
E17	1668	-0.2791	0.3206	0.5997	$1.33 \cdot 10^{-4}$	$9.94 \cdot 10^{-2}$

in data set E01. Finally, the range of the signal appears to be close to the 0.6 level for the first six data sets, considerably larger for the subsequent ten data sets, returning to the 0.6 level for E17.

There are also places in the data sets where successive measurements appear to be in a perfect linear relationship, e.g., see files E02, E03, E04, E07, E09, E12, E14, and E17. One explanation of this effect may involve the removal of the background, as described on p. 327 of Ref. [2]: "... [W]e interrupted

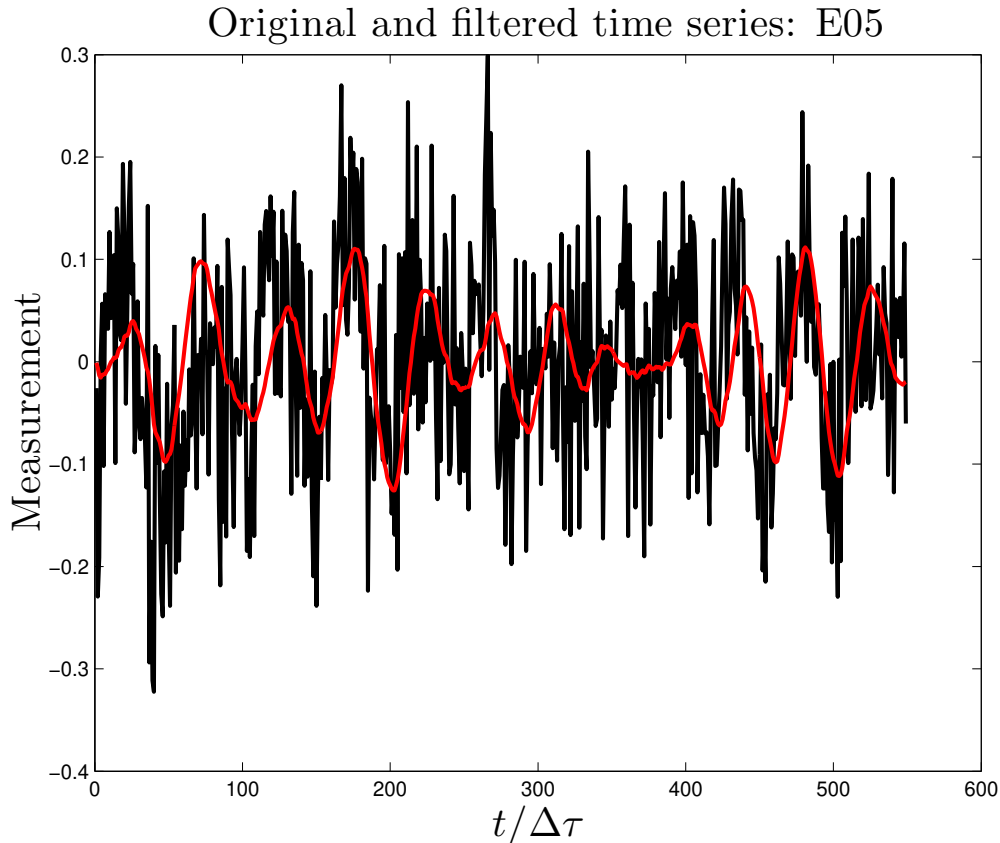


Fig. 1. The luminosity measurements contained in the data set E05 of Ref. [10]. The plot is shown as an extreme example of the amount of noise contained in the measurements of the pre-white dwarf PG 1159-035 available from Ref. [10]. The measurements are connected with black line segments, whereas the filtered data (see Section 4) correspond to the red curve.

the observations of the target and comparison star for about 1 minute of sky observations at regular intervals of roughly 20 minutes (when the Moon was up and the sky was very bright) to 1 hr (a more typical value since the bulk of the observations were obtained during dark-time). We then interpolated linearly between sky observations and subtracted the result from the data.”

3 The analysis of the original time-series arrays

The analysis of the time-series arrays of Ref. [10] will generally follow the guidelines of the book ‘Nonlinear Time Series Analysis’ by Kantz and Schreiber [12], a book which (in my opinion) should be of interest even to those who do not intend to perform non-linear analyses; for brevity, I will refer to these two authors as ‘KS’ from now on. The stationarity of each time series of

measurements is tested on the basis of the variation of the average and of the rms values of the measurements contained in successive data segments (of the given time series of measurements). The spectrogram is also analysed. If N stands for the total number of measurements in a data set, W for the length of the running windows (expressed in sampling intervals), $S \leq W$ for the shift of the window (also expressed in sampling intervals) in successive positions, n for the number of windows, and r for the total number of unpaired measurements (i.e., of the data points which are not included in any window), the relation arises:

$$N = (n - 1)S + W + r .$$

Therefore, $r = N - (n - 1)S - W$. By varying S and W within user-defined limits (5% limits are adopted in this work), starting from a 5% overlap ($d = 1 - S/W$) between successive windows, one may minimise r separately for each time series, thus excluding (in the test of stationarity) as few measurements as possible. A few measurements are excluded only in the test of stationarity of the input time series, i.e., not in Section 5 where the dynamical invariants of the source of the observations are determined.

For the detection of the outliers in the sets of the average and of the rms values, Rosner's generalised ESD (Extreme Studentised Deviate) test [13] was performed. In this algorithm, a set of N_k values is tested for the presence of exactly 1, 2, ..., N_a outliers, where N_a is a user-defined limit satisfying the condition $N_a < N_k$ (the test is performed for $N_a \leq \lfloor N_k/3 \rfloor$). The advantage of Rosner's test (in comparison to other tests, e.g., to Grubbs's outlier test [14,15]) is that the 'optimal' number of outliers is obtained from the input data themselves. In addition, a χ^2 test was performed on the set of the average values and their uncertainties (i.e., the standard error of the means) corresponding to each window: for a set of n independent³ measurements x_i , with uncertainties δx_i , the χ^2 value associated with the reproduction of the measurements by their weighted average is given by:

$$\chi^2 = \sum_{i=1}^n w_i x_i^2 - \left(\sum_{i=1}^n w_i x_i \right)^2 / \sum_{i=1}^n w_i , \quad (1)$$

where the weight w_i is equal to $(\delta x_i)^{-2}$. The comparison of the p-value, obtained from the χ^2 of Eq. (1) and the number of degrees of freedom $n - 1$ (one degree of freedom needs to be removed, as the constant of the reproduction of the input values is extracted from the values themselves), with a user-defined significance threshold p_{\min} enables the test of the constancy of the input values x_i : the constancy is accepted when $p \geq p_{\min}$, rejected when $p < p_{\min}$. In ac-

³ Of course, unless the overlap between successive windows vanishes, the x_i values are not independent. However, the average overlap between successive windows in this work was about 6.2%, i.e., low enough to enable one to 'gloss over' the issue of independence.

cordance with the choice of most statisticians, the p_{\min} threshold of $1.00 \cdot 10^{-2}$ was adopted herein as the outset of statistical significance.

I will next address some of the properties of the autocorrelation function⁴. This function enables the extraction of an estimate for the embedding delay, which is one of the two important quantities in the reconstruction of the phase space (state space, for others) of the dynamical system yielding the time-series measurements, i.e., of the vector space within which the system ‘lives’. One important step when extracting estimates for the dynamical invariants of a non-linear system is the exclusion of the elements of the time series which are ‘temporally correlated’ with a given element s_k ; their closeness to s_k is due to the frequency at which the dynamical system is being observed⁵. Such elements are not only superfluous in the context of time-delay embeddings; they actually obscure the geometrical features of the phase space. The determination of the embedding delay is the first step in a time-series analysis. In this work, the embedding delay will be expressed in sampling intervals: therefore, the embedding delay ν represents the temporal interval $\nu\Delta\tau$.

The second important quantity in time-delay embeddings is the dimension m of the embedding vectors⁶. Given an element with index $i > (m - 1)\nu$ of the original time-series array s_k ($k \in \{1, \dots, N\}$), the components of the embedding vectors β_i are suitably chosen elements of the series, representing epochs which end at the time instant i :

$$\beta_i := (s_{i-(m-1)\nu}, s_{i-(m-2)\nu}, \dots, s_{i-\nu}, s_i) . \quad (2)$$

Therefore, each time instant $i\Delta\tau$ may be associated with an m -dimensional

⁴ Although the term ‘autocorrelation function’ is routinely used in the analysis of discrete time series, it is technically more appropriate to refer to the autocorrelation as a ‘sequence’. To retain simplicity however, I will also use the term ‘autocorrelation function’ in this work, assume that a function is obtained from the sequence by interpolation, and refrain from introducing new terminology for the mere sake of formality.

⁵ To understand the removal of these temporally correlated elements, consider that, while driving your vehicle, you arrive at a four-way intersection (two perpendicular roads). Let me denote the four roads, starting at the intersection, as A, B, C, and D. The motion of the vehicle is defined if one sets the direction from which it reaches the intersection (e.g., C) and the one it follows after it (e.g., A). If one is not interested in providing estimates for the instantaneous velocity of the vehicle, all other observations (of the position of the vehicle as a function of time) are redundant.

⁶ In fact, it is pointed out in the literature that the most important parameter in time-delay embeddings is the *time span of the embedding vectors*, namely the product $m\nu$ or equivalently the length of the embedding time window $m\nu\Delta\tau$. Nevertheless, I will follow the ‘traditional’ approach herein, and regard m and n as the free parameters.

vector with (for an appropriate choice for the lag) independent components. The study of these m -dimensional vectors β_i enables the extraction of the important information, i.e., of the characteristics of the phase space of the dynamical system.

The unbiased variance of the measurements of a time series is given by the expression:

$$\hat{\sigma}^2 = \frac{1}{N-1} \sum_{i=1}^N (s_i - \langle s \rangle)^2 ,$$

where

$$\langle s \rangle = \frac{1}{N} \sum_{i=1}^N s_i .$$

The unbiased variance at lag j is defined as

$$\hat{\sigma}_j^2 = \frac{1}{N-1-j} \sum_{i=j+1}^N (s_{i-j} - \langle s \rangle_j)(s_i - \langle s \rangle_j) ,$$

where the quantity $\langle s \rangle_j$ will be obtained from the variation of $\hat{\sigma}_j^2$. It may be proven that $\hat{\sigma}_j^2$ is minimal when

$$\langle s \rangle_j = \frac{1}{2(N-j)} \sum_{i=j+1}^N (s_i + s_{i-j}) .$$

Finally,

$$\hat{\sigma}_j^2 = \frac{1}{N-1-j} \left(\sum_{i=j+1}^N s_{i-j} s_i - (N-j) \langle s \rangle_j^2 \right) .$$

The autocorrelation at lag j is defined as the ratio $\hat{\sigma}_j^2 / \hat{\sigma}_0^2 \equiv \hat{\sigma}_j^2 / \hat{\sigma}^2$. Therefore, the autocorrelation at lag 0 is identically equal to 1.

The autocorrelation function may provide information on the nature of the input time series. For instance, it is known that white noise has a random autocorrelation function, whereas signals from deterministic chaotic systems yield exponentially-decaying autocorrelation functions. KS favour the fixation of the embedding delay from the first root of the autocorrelation function (this option is also followed here). Another choice, presumably more suitable for the analysis of time series yielding slowly-decaying autocorrelation functions, would be to use the time at which the autocorrelation function drops (for the first time) below the value of e^{-1} . (Of course, there are other possibilities, e.g., to use the first minimum of the mutual-information function.) An evident question arises: if the emphasis is placed on the independence of the elements of the embedding vectors, why should one not simply choose an embedding delay considerably larger than the lag? The answer is that the choice of an ‘economical’ embedding delay prevents the unfolding of the attractor (of a dissipative chaotic system) onto itself.

After these explanations, it is time I came to the results of the analysis of the seventeen original time-series arrays obtained from the pre-white dwarf PG 1159-035 (see Table 2). The dominant frequency present in the measurements is equal to about 4% of the Nyquist frequency, i.e., about 2 mHz, corresponding to a period of about 500 s. To be able to test the stationarity of the input time series using an adequate amount of measurements⁷, it was decided to make use of windows (initial value, subject to 5% variation in order to minimise r) spanning two periods of the dominant oscillation in the signal, covering about 1000 s. This is the reason that the windows in Table 2 have a length of about 100 sampling intervals.

Significant departure from stationarity is seen in all cases in Table 2: there is no data set in which the stationarity of the signal can be asserted. In several cases, the Discrete Fourier Transform is enhanced at low frequencies, implying that the original time series exhibits long-term oscillations⁸; presumably, such effects do not have much to do with the system under observation. The long-term oscillations directly affect the autocorrelation function, leading to the extraction of longer embedding delays. (Of course, the enhanced low-frequency components in the power spectrum and the stationarity of the input data do not easily come to terms.) Inspection of Table 2 leaves little doubt that, in order to be of use, the available measurements must first be filtered.

⁷ Regarding the tests of stationarity in a time series, Refs. [12] emphasise: “. . . the time series should cover a stretch of time which is much longer than the longest characteristic time scale that is relevant for the evolution of the system.” Although the definition of “much longer” is subjective, it is unlikely that the time-series arrays analysed in this work qualify as “long enough”, and even more so the running windows used in the test of stationarity (which are only double the size of the dominant time scale). I would have preferred to use longer windows (e.g., 500 sampling intervals), but this would not have worked on most of the snippets of Ref. [10].

⁸ On p. 629, the authors of Ref. [3] put forward an explanation for the enhanced low-frequency (below 300 μ Hz), high-amplitude peaks in the Fourier spectrum, attributing their appearance to atmospheric phenomena, yielding corrections which are dependent on the colour of a star. As a result, a calibration obtained from a close-by (comparison) star of a different surface temperature (to the one of the target object) introduces spurious effects in the frequency spectrum of the object of interest.

Table 2

Some quantities relating to the analysis of the original luminosity measurements of PG 1159-035. W is the length of the running window, S its shift, and ν the embedding delay (first zero of the autocorrelation function); all these quantities are expressed in sampling intervals $\Delta\tau$. The quantity d is the overlap between successive windows, n is the number of windows, and r stands for the number of unpaired points (i.e., for those which are not contained in any window); measurements are excluded only in the test of stationarity of each input time series. The column ‘p-value’ contains the p-value pertaining to the test of stationarity (constancy of the average signal within each running window), obtained from the χ^2 value of Eq. (1) and the number of degrees of freedom $n - 1$. LFC stands for ‘Low-Frequency Components’ and ‘DFT’ for ‘Discrete Fourier Transform’.

Data set	W	S	d (%)	n	r	p-value	ν	Comments
E01	105	100	5	6	12	$2.54 \cdot 10^{-3}$	14	Transient effects in first 100 steps
E02	103	96	7	13	0	$2.34 \cdot 10^{-14}$	14	Trough in the middle of the data set
E03	105	93	11	13	0	≈ 0	15	
E04	105	97	8	10	1	≈ 0	18	
E05	99	90	9	6	0	$9.40 \cdot 10^{-3}$	13	No obvious structure in the data
E06	97	91	6	17	0	$8.66 \cdot 10^{-5}$	14	
E07	96	92	4	21	0	≈ 0	26	Enhanced LFC in DFT; slowly-decaying autocorrelation function
E08	103	92	11	27	0	≈ 0	15	
E09	97	97	0	20	0	$6.01 \cdot 10^{-14}$	14	
E10	99	98	1	15	0	≈ 0	15	

4 The filtering of the time-series arrays

Despite the fact that Refs. [2,3] read with pleasure, I am not sure that I grasp the application of the corrections to the raw data⁹. Some remarks on the data processing may be found on pp. 327–329 of Ref. [2]: “The effects of extinction and other slow transparency variations were accounted for by fitting a third-degree polynomial to each sky-subtracted data set and then dividing by this fit. This also normalised the data, so we then subtracted 1 to give a mean of zero for all the data sets. This procedure yields a light curve with variation

⁹ Both papers refer to earlier work as to the processing of the raw measurements. I have not read these earlier papers.

Table 2 continued

Data set	W	S	d (%)	n	r	p-value	ν	Comments
E11	105	100	5	26	0	≈ 0	129	Enhanced LFC in DFT; oscillating autocorrelation function
E12	105	90	14	17	3	≈ 0	17	Enhanced LFC in DFT; peculiar peak in DFT at about 8.4 mHz
E13	98	95	3	27	0	≈ 0	15	Enhanced LFC in DFT
E14	102	100	2	26	0	$6.43 \cdot 10^{-8}$	14	
E15	96	96	0	7	0	≈ 0	68	Enhanced LFC in DFT; oscillating autocorrelation function; trough in the middle of the data set; effects in last 100 steps
E16	102	94	8	16	0	≈ 0	72	Enhanced LFC in DFT; oscillating autocorrelation function; trough in the middle of the data set
E17	104	92	12	18	0	≈ 0	19	Enhanced LFC in DFT

in amplitude as a function of the total intensity; such reduced light curves from different sites can then be combined without further processing. We used the data obtained on a nearby comparison star in channel 2 to measure sky transparency. Data contaminated by cloud were discarded. The final product of these basic reduction procedures is shown in [their] Fig. 1, the light curve of the 6.5 day interval when all the observatories were online. Note that the overlaps - where data were obtained simultaneously at two sites at different longitude - are visible only by the increased density of points; there are no discontinuities in the light curve that arose from ‘stitching’ the runs from individual sites into the composite whole.” On p. 629 of Ref. [3], one reads that the authors “fitted a polynomial of 4-th order to the light curve of each individual night, but even so, residual frequencies with considerable amplitude persisted in the residual light curve.” The authors conclude: “To eliminate them, we used a *high-pass* filter, an algorithm that detects and eliminates signals with high amplitudes and frequencies lower than 300 μHz .”

In relation to the pulsation modes of PG 1159-035, Refs. [2,3] make it clear that the range of interest (in frequency) lies between 1 and 3 mHz. This may be taken to suggest that the contributions (to the variation of the luminosity of PG 1159-035) from frequencies outside this range do not originate from g -wave

pulsations, but are due to other (uninteresting in the context of these works) phenomena. Evidently, one way to suppress the influence of such phenomena is by band-passing the original time series. The validity of this filtering procedure (e.g., the choice of the corner frequencies) rests upon our understanding of the physical processes underlying the observations of the physical system, namely of the way in which the ultra-dense matter behaves.

The following questions are relevant in case of application of a band-pass filter:

- Which is the best filtering method in the particular problem?
- Which filtering order should be used?
- Which are the band-pass corner frequencies?
- Which are the band-stop corner frequencies?
- How large should the band-pass ripple be?
- How large should the band-stop attenuation be?

Although some of these questions can be answered by methods contained in my C/C++ library, it is more convenient (and often faster) to use MATLAB[®] (The MathWorks, Inc., Natick, Massachusetts, United States) in filtering applications; I used MATLAB 7.5.0 in this work. Four filtering methods have been examined: Butterworth, Chebyshev (types I and II), and elliptic filters. In each case, the best filtering order was obtained from the desired band-pass/stop corner frequencies, the band-pass ripple, and the band-stop attenuation, using the MATLAB methods `buttord`, `cheb1ord`, `cheb2ord`, and `ellipord`, corresponding to the four aforementioned filtering methods, in that order. The application of the best filter was then enabled with the use of the MATLAB methods `butter`, `cheby1`, `cheby2`, and `ellip`, corresponding again to the four aforementioned filtering methods, in that order.

The left and right band-pass frequencies were set equal to 1 and 3 mHz, respectively. The left and right band-stop frequencies were set equal to 0.5 and 3.5 mHz, respectively. A few options were examined in relation to the band-pass ripple and the band-stop attenuation. By decreasing the former, one obtains filter response functions which vary less in the band-pass region; by increasing the latter, one obtains filter response functions which vary less in the band-stop region. Evidently, the ideal filter would result in a vanishing band-pass ripple and in complete band-stop attenuation. Of course, the ideal filter is a fictitious concept. In an effort to obtain filters which resemble better the ideal one, one may try to suppress the band-pass ripples and increase the band-stop attenuation, yet the order of the required filter increases the closer it comes to the ideal filter. In applications, this is not only time-consuming, but also prone to instability. Last but not least, high-order filters usually generate more delay between the original and the filtered data. Evidently, the selection of the best filter is a trade-off process between the ideal (application of Heaviside step functions) and the practical (stability, acceptable delay)

filtering. The investigation suggested the use of the following parameters.

- Peak-to-peak band-pass ripple: 10%, corresponding to about -0.915 dB.
- Peak-to-peak band-stop attenuation: 90%, corresponding to -20 dB.

(The unit dB stands for ‘decibel’.) The peak-to-peak band-pass ripple of 10% allows the filter response function to vary in the band-pass region between 90% and 100% of the peak value; the peak-to-peak band-stop attenuation of 90% forces the filter response function to remain below 10% of the peak value in the band-stop region. Even with these loose conditions, the Butterworth filter did not produce stable results. The results obtained with the remaining three filtering methods (see Fig. 2) were found acceptable. The elliptic filter was finally chosen, as it required the lowest order (6-th), thus achieving the filtering of the time-series arrays with 13 recursion coefficients. (For the Chebyshev type I and II filtering methods, 10-th order filters were suggested, whereas the failing Butterworth method required a 22-nd order filter.)

In Infinite Impulse Response (IIR) digital filtering, an M -order filter, applied (left-to-right) to the input time series, follows the recurrence relationship¹⁰ :

$$y_i = a_0 x_i + \sum_{k=1}^M (a_k x_{i-k} - b_k y_{i-k}) \quad (3)$$

where x_i stands for the input time-series array, y_i for the filtered array. The constants a_k and b_k are known as recursion coefficients. (More general forms have appeared in the literature, e.g., allowing for different dimensions of the two arrays of recursion coefficients.) The coefficients of the elliptic filter, applied to the original time-series arrays of this work, are given in Table 3.

The seventeen time series of Ref. [10] were submitted to this filtering procedure. The properties of the resulting time series are given in Table 4. Many discrepancies, observed when processing the original data, have disappeared. It is comforting to see that the values of the embedding delay ν come out consistent after the filtering, namely between 12 and 14 sampling intervals in all cases. In short, the luminosity measurements of PG 1159-035 may be considered temporally uncorrelated if separated by slightly over 2 minutes. Equally comforting is the assertion of the stationarity of the observations, as revealed by the p-values, obtained from the χ^2 of Eq. (1) and the number of degrees of freedom $n - 1$ in each data set; all p-values exceed the significance threshold p_{\min} of this work ($1.00 \cdot 10^{-2}$).

¹⁰ The role of the recursion coefficients a and b frequently appears interchanged in the literature. I consider it more ‘natural’ to apply the coefficients a to the original data and the coefficients b to the filtered ones.

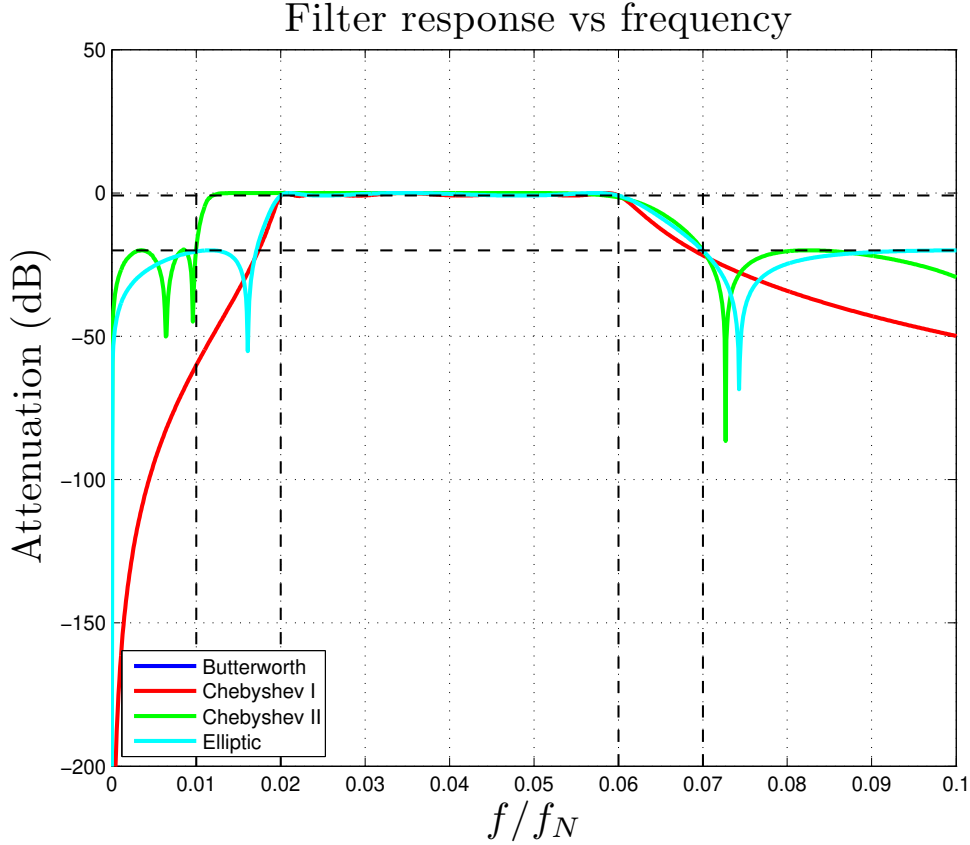


Fig. 2. A comparison of the response functions obtained with the Chebyshev type I, the Chebyshev type II, and the elliptic filters for the filter properties given in Section 4. The Butterworth filtering method was also examined, but the results were not reasonable and are not shown in the figure. The Nyquist frequency f_N for the measurements of PG 1159-035 is equal to 50 mHz.

5 The analysis of the filtered time-series arrays

5.1 Creation of a database of embedding vectors

To determine whether the physical processes, underlying the observations, are linear or non-linear, one needs to perform a non-linear analysis of the measurements. Each element of a time series may be considered as an instance of the ‘present’; the preceding elements may be thought of as representing the element’s ‘past’, whereas subsequent ones its ‘future’. Therefore, in a given time series, the past and the future of each ‘snapshot of the present’ are known (of course, the extent to which the past and the future of an element are known depends on the position of that element in the time series), save for the first element (whose past is unknown) and the last one (whose future is unknown).

Table 3

The recursion coefficients (see Eq. (3)) of the elliptic filter used in band-passing the original time-series arrays of this work.

Recursion coefficient	Value
a_0	$1.936650845443 \cdot 10^{-2}$
a_1	$-7.636547752052 \cdot 10^{-2}$
a_2	$9.463412534230 \cdot 10^{-2}$
a_3	$6.020320205958 \cdot 10^{-17}$
a_4	$-9.463412534230 \cdot 10^{-2}$
a_5	$7.636547752052 \cdot 10^{-2}$
a_6	$-1.936650845443 \cdot 10^{-2}$
b_1	$-5.827902199708 \cdot 10^0$
b_2	$1.419838266997 \cdot 10^1$
b_3	$-1.850916256654 \cdot 10^1$
b_4	$1.361687656364 \cdot 10^1$
b_5	$-5.360263930430 \cdot 10^0$
b_6	$8.820710201218 \cdot 10^{-1}$

The determination of whether a system is linear or non-linear rests upon the extraction of predictions from the known past of each element of the time series and their subsequent comparison to the measurements representing that element's future. To this end, a database of embedding vectors was created, along with the associated predictions for $\Delta n = 100$ sampling intervals into the future of the last element of each such vector. A time-series array containing N elements yields $N - \Delta n - (m - 1)\nu$ embedding vectors. The predictions, obtained from the database of embedding vectors, will be used for estimating the out-of-sample prediction errors.

The data sets were split into two parts: one part yielded the training (or learning) set, from which the database embedding vectors were obtained, the other the test set, which provided the vectors, whose neighbours are sought among the database entries. These two independent sets were created as follows. The seventeen data sets of Table 4 were first ordered in terms of the number of measurements they contain. The data set with the largest content (i.e., the data set E11) was assigned to the training set. Each subsequent pair of files were assigned either to the test or to the training sets alternatively (starting with the test set) until seven data sets had been selected for the training set. The last four files were assigned to the test set. Selected for the training set

Table 4

Some quantities relating to the filtered time-series arrays of PG 1159-035. The filtering of the original measurements is discussed in Section 4.

Data set	s_{\min}	s_{\max}	$s_{\max} - s_{\min}$	$\langle s \rangle$	rms	p-value	ν
E01	-0.2419	0.2425	0.4844	$3.026 \cdot 10^{-4}$	$1.156 \cdot 10^{-1}$	$9.82 \cdot 10^{-1}$	14
E02	-0.1957	0.2162	0.4119	$-4.645 \cdot 10^{-5}$	$8.181 \cdot 10^{-2}$	$9.24 \cdot 10^{-1}$	13
E03	-0.1624	0.1493	0.3117	$1.018 \cdot 10^{-4}$	$7.037 \cdot 10^{-2}$	$8.07 \cdot 10^{-1}$	13
E04	-0.1401	0.1680	0.3081	$1.210 \cdot 10^{-4}$	$7.372 \cdot 10^{-2}$	$4.95 \cdot 10^{-1}$	14
E05	-0.1257	0.1117	0.2374	$-1.590 \cdot 10^{-4}$	$5.111 \cdot 10^{-2}$	$7.14 \cdot 10^{-1}$	12
E06	-0.1822	0.2029	0.3850	$1.125 \cdot 10^{-4}$	$7.212 \cdot 10^{-2}$	$6.50 \cdot 10^{-1}$	13
E07	-0.2279	0.2147	0.4426	$4.551 \cdot 10^{-5}$	$8.888 \cdot 10^{-2}$	$5.39 \cdot 10^{-2}$	14
E08	-0.3259	0.3286	0.6544	$-7.094 \cdot 10^{-5}$	$1.206 \cdot 10^{-1}$	$6.59 \cdot 10^{-1}$	13
E09	-0.3340	0.3340	0.6680	$5.784 \cdot 10^{-5}$	$1.141 \cdot 10^{-1}$	$3.12 \cdot 10^{-1}$	14
E10	-0.3270	0.3083	0.6352	$6.431 \cdot 10^{-5}$	$1.179 \cdot 10^{-1}$	$4.29 \cdot 10^{-1}$	14
E11	-0.2179	0.2829	0.5008	$1.190 \cdot 10^{-2}$	$9.538 \cdot 10^{-2}$	$4.98 \cdot 10^{-2}$	14
E12	-0.2609	0.2379	0.4988	$6.363 \cdot 10^{-5}$	$8.584 \cdot 10^{-2}$	$4.23 \cdot 10^{-1}$	13
E13	-0.2784	0.2716	0.5499	$-5.841 \cdot 10^{-7}$	$9.428 \cdot 10^{-2}$	$1.24 \cdot 10^{-1}$	13
E14	-0.2750	0.2583	0.5333	$-1.653 \cdot 10^{-3}$	$9.867 \cdot 10^{-2}$	$5.20 \cdot 10^{-2}$	13
E15	-0.2979	0.2112	0.5090	$-3.384 \cdot 10^{-4}$	$9.970 \cdot 10^{-2}$	$6.16 \cdot 10^{-1}$	14
E16	-0.2222	0.2414	0.4636	$5.221 \cdot 10^{-3}$	$8.770 \cdot 10^{-2}$	$5.11 \cdot 10^{-1}$	13
E17	-0.1640	0.1686	0.3327	$1.327 \cdot 10^{-4}$	$6.247 \cdot 10^{-2}$	$3.05 \cdot 10^{-1}$	13

were the data sets: E11, E08, E09, E06, E12, E02, and E03. Selected for the test set were the data sets: E14, E13, E07, E17, E16, E10, E04, E15, E01, and E05. As a result, 12617 measurements in total were assigned to the training set, 14574 to the test set. The distributions of the minimal and maximal signals, of the range, of the average, and of the rms values between the two sets were subjected to tests for significant differences (two-tailed, homoscedastic t-tests); none were found.

Given that the seventeen data sets represent luminosity measurements of a stationary (during the temporal span of the observations) process, it makes sense to use one lag value ν in the analysis. This choice is not a matter of convenience, but one of rationality. (In fact, the implementation has been made in such a way that it covers the general case, i.e., variable lag.) The

maximal lag from Table 4, namely $\nu = 14$, will be used in the remaining part of this paper. As any two luminosity measurements are assumed independent if temporally separated by ν sampling intervals, the choice of the maximal lag value in Table 4 ensures that the components of all embedding vectors, be they related to the training or to the test set, will be independent.

5.2 Distance in an m -dimensional space

Before advancing, one word about the definition of the distance d between two m -dimensional vectors a_k and b_k is due. The general definition of the distance is:

$$d = \left(\sum_{k=1}^m |a_k - b_k|^n \right)^{1/n} ,$$

where $n = \{1, \dots, +\infty\}$ sets the norm. The Euclidean distance corresponds to $n = 2$ (L^2 distance). The L^1 -norm distance is the sum of the absolute values of the differences between the components of the two vectors

$$d = \sum_{k=1}^m |a_k - b_k| ,$$

whereas the L^∞ -norm distance satisfies

$$d = \max\{|a_k - b_k|\}_{k=1}^m . \quad (4)$$

Although the main results of this work will be obtained with the L^∞ distance, use of the L^2 distance will also be made, as a verification step, in Section 5.7.

5.3 On the optimal embedding dimension and range of variation of the neighbourhood size

As mentioned in Section 3, the determination of the optimal embedding dimension is an important step in phase-space reconstructions. If the dimensionality of the phase space is D , Takens' theorem [16] ensures that embeddings exist in a mathematical space of more than $2D$ dimensions, which fully uncover the characteristics of the phase space. Takens' theorem does not *prohibit* sufficient embeddings in fewer dimensions¹¹; it simply does not *guarantee* their

¹¹ To mention two examples: the correlation dimension (to be introduced in Section 5.5) for the attractor of the Hénon map has been estimated to 1.25 ± 0.02 [17], yet the optimal embedding dimension is 2 [18]; for the Lorenz attractor, the correlation dimension has been estimated to 2.05 ± 0.01 [17] and the optimal embedding dimension is 3 [18].

existence. In any case, the minimal embedding dimension, leading to a sufficient embedding, will be called optimal from now on (and will be denoted by m_0). Obviously, the use of embedding dimensions below the optimal one yields embeddings which are insufficient: they cannot cover the phase space.

As when addressing the optimal embedding delay in Section 3, one question arises: if the objective is to obtain sufficient embeddings, why should one not choose an embedding dimension so large that the probability of an insufficient embedding be practically zero? The answer is that large embedding dimensions introduce complexity and redundancy, and hinder the interpretation of the results of an analysis. KS give two additional arguments: large embedding dimensions demand large computational effort (which became less of a problem during the last two decades) and (more importantly) they lead to the degradation of the performance of the algorithms used in non-linear analysis.

A number of methods have been put forward to provide a reliable estimate for the optimal embedding dimension. One category of methods pivot on the technique of the ‘false nearest neighbours’ (FNN), introduced by Kennel, Brown, and Abarbanel in 1992 [19]. The idea behind the method is quite simple. As m_0 is the optimal embedding dimension, the set of embedding vectors, neighbouring an arbitrary vector, is expected to be left intact in embeddings in $m_0 + 1$ dimensions. In case of an insufficient embedding (i.e., when $m < m_0$), all embedding vectors, corresponding to the true neighbours in the m_0 -dimensional embedding, will also be contained in the set of neighbours in the m -dimensional embedding; this is guaranteed by the definition of the neighbourhood. However, given that the m -dimensional embedding is not the optimal one, m_0 -dimensional vectors exist which, though not belonging to the neighbourhood in m_0 dimensions, are projected onto neighbouring vectors in the m -dimensional embedding. These are the false neighbours, i.e., states which are ostensibly neighbouring (a specific state) only because the embedding dimension is insufficient.

Several variants of the FNN method have appeared in the literature, e.g., see Refs. [12,18,20] (this list is anything but exhaustive). Cao’s method [18] is my favourite for three reasons: a) it is a parameter-free approach (save for the lag), b) it is straightforward to implement, and c) it is robust. In Section 5.4, I will obtain an estimate for the optimal embedding dimension of the luminosity measurements of PG 1159-035 using this method. Another category of methods involve the m -dependence of a dynamical invariant, i.e., of a quantity characterising the phase space, e.g., of the correlation dimension or of the maximal Lyapunov exponent. Interesting overviews on this subject may be found in Refs. [18,20], as well as in the works cited therein.

The choice for the neighbourhood size ϵ , entering the determination of the correlation dimension and the extraction of the maximal Lyapunov exponent,

is addressed in Refs. [12]. As there is no concrete, theoretically justified way to select ϵ , the determination of the appropriate range of values remains, to a large extent, empirical; frequently, the trial-and-error method is the only practical approach. KS write: “Studies with known true signals suggest that a good choice for the neighbourhood size is given by 2 – 3 times the noise amplitude.” However, this recommendation cannot easily be followed if a noise-reduction scheme has been applied to the input data. As a remedy against the lack of a concrete theoretical basis for the determination of the ϵ domain, KS suggest the use of several ϵ values, and frequently in their book they vary ϵ within a range covering a few orders of magnitude. Evidently, ϵ may be thought of as a free parameter in a non-linear analysis: KS recommend that the only prerequisite in the variation of ϵ be the existence of an adequate number of neighbours within the m -dimensional balls (or boxes) corresponding to the different embeddings.

The average rms of the measurements of PG 1159-035 (filtered time-series arrays) is equal to about $9.00 \cdot 10^{-2}$, see Table 4. It was decided to use half the average rms as the starting value of ϵ , and decrease this parameter (using a small step) until the number of neighbours dropped to such a level that the statistical analysis was possible only for low-dimensional embeddings (e.g., below 6).

5.4 *Cao’s method for the determination of the optimal embedding dimension*

In the abstract of his 1997 paper, Cao lists the advantages of his method for determining the optimal embedding dimension: the method “(1) does not contain any subjective parameters except for the time-delay for the embedding; (2) does not strongly depend on how many data points are available; (3) can clearly distinguish deterministic signals from stochastic signals; (4) works well for time series from high-dimensional attractors; (5) is computationally efficient.”

Using the L^∞ distance, Cao’s method examines the dependence of two quantities, named $E1$ and $E2$ in the paper (see Eqs. (1 – 5) in Ref. [18]), on the embedding dimension: $E1$ represents the relative change of the average distance between neighbouring embedding vectors when increasing the embedding dimension by one unit, whereas $E2$ essentially tests the independence of past and future values. As Cao remarks, his method distinguishes deterministic and stochastic signals: in the latter case, $E2$ comes out close to 1 regardless of the embedding dimension. For deterministic signals, $E1$ and $E2$ approach saturation with increasing embedding dimension: the optimal embedding dimension is chosen to be the one at which $E1$ saturates, i.e., it does not change (significantly) when further increasing m . Cao recommends the evaluation and visual

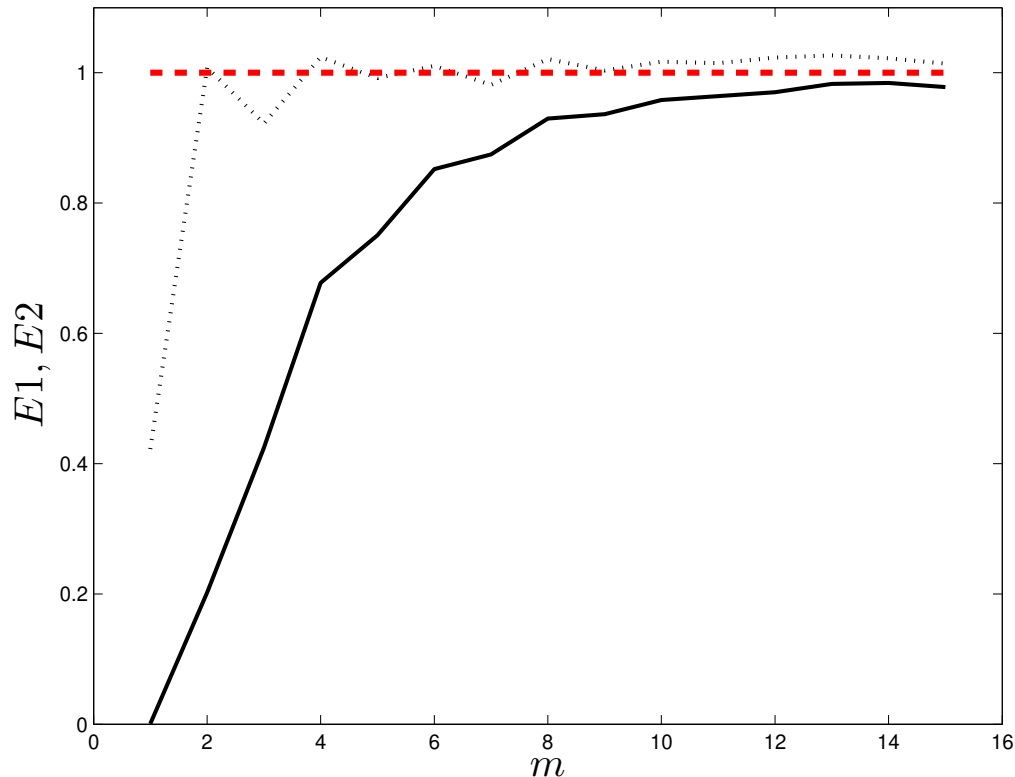


Fig. 3. Cao’s $E1$ (straight line segments) and $E2$ (dotted line segments) for embedding dimensions m up to 15. The training and test sets, as defined in Section 5, have been used.

inspection of $E2$, as the means to ensure that the signal analysed is indeed deterministic.

The quantities $E1$ and $E2$ were evaluated for embedding dimensions up to $m = 15$, using (as the only input) $\nu = 14$, and the training and test sets, as defined in Section 5. The results are shown in Fig. 3.

Although one extracts a large estimate for the optimal embedding dimension from Fig. 3, perhaps around 13, it might make sense to accept that $E1$ already saturates in the vicinity of 10. This choice is confirmed by the result of the separate analysis¹² of the seventeen input data sets, shown in Fig. 4. There is general agreement between Figs. 3 and 4: from these two figures, it appears

¹²To reduce the temporal correlations in the separate analysis of the data sets, all contributing (to the determination of $E1$ and $E2$) embedding vectors were required to have a temporal separation (constant distance between their corresponding elements) exceeding the embedding delay ν . Temporal separations of $2\nu\Delta\tau$ and $3\nu\Delta\tau$ have also been attempted, but induced very small differences on the results.

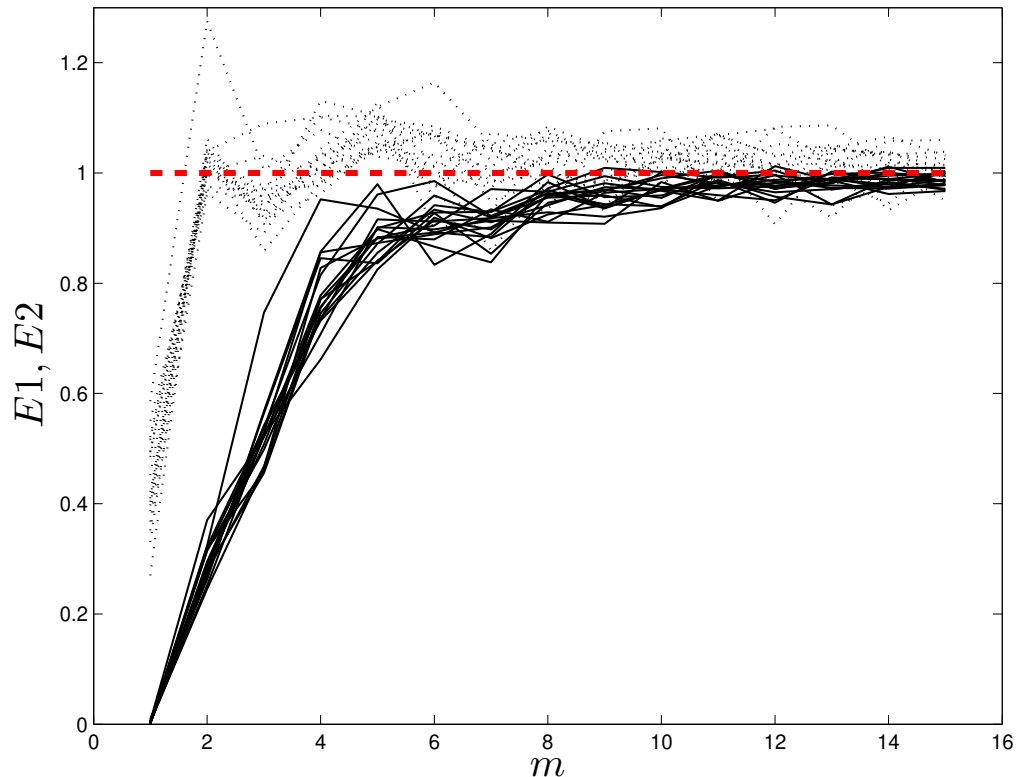


Fig. 4. Cao’s $E1$ (straight line segments) and $E2$ (dotted line segments) for embedding dimensions m up to 15. These quantities have been obtained from a separate analysis of the seventeen data sets (no splitting of the data into training and test sets). All contributing embedding vectors were required to have a temporal separation exceeding $\nu\Delta\tau$.

reasonable to accept the value of 10 as the optimal embedding dimension.

5.5 Correlation dimension

The notion of the correlation dimension was introduced by Grassberger and Procaccia in 1983 [17]: it is a measure of the dimensionality of the phase space. Let us examine how the correlation dimension is obtained from the correlation sum, which represents the frequentness of embedding vectors in the time series whose distance is below a given neighbourhood size ϵ :

$$C(\epsilon) = \frac{2}{N(N-1)} \sum_{i=1}^{N-1} \sum_{j=i+1}^N \Theta(\epsilon - \|\mathfrak{B}_i - \mathfrak{B}_j\|) , \quad (5)$$

where $\Theta(x)$ is the Heaviside step function, attaining the values of 0 when $x < 0$, and 1 when $x \geq 0$. To suppress the temporal correlations, KS propose a modification of Eq. (5):

$$C(\epsilon) = \frac{2}{(N - n_{\min})(N - 1 - n_{\min})} \sum_{i=1}^{N-1-n_{\min}} \sum_{j=i+1+n_{\min}}^N \Theta(\epsilon - \|\beta_i - \beta_j\|) , \quad (6)$$

and recommend the use of a generous n_{\min} , significantly exceeding the lag extracted from the autocorrelation function. (The expressions, given by KS in both editions of their book, need to be corrected: the upper limits of the first sums are misleading. In addition, one unit must be added to the lower limit of the second sum of the equation featuring n_{\min} in the first edition. Equations (5,6), as they appear in this work, are the correct expressions.)

It is expected that, in the limit $N \rightarrow \infty$, $C(\epsilon)$ would scale like a power law at small ϵ values, i.e., $C(\epsilon) \sim \epsilon^D$. The correlation dimension D would thus be obtained as a double limit.

$$\alpha(N, \epsilon) = \frac{\partial \ln C(\epsilon)}{\partial \ln \epsilon} \quad (7)$$

$$D = \lim_{N \rightarrow \infty} \lim_{\epsilon \rightarrow 0} \alpha(N, \epsilon)$$

The practical application of these notions to a time series involves the stability of $\alpha(N, \epsilon)$ when plotted as a function of ϵ for several embedding dimensions. KS remark that the estimation of the correlation dimension should be thought of as a two-step process. In the first step, the correlation sums are evaluated for several ϵ and m values. The second step involves the visual inspection of the $(\ln \epsilon, \ln C(\epsilon))$ scatter plots: if an ϵ domain exists, within which the dependence of $\ln C(\epsilon)$ on $\ln \epsilon$ is linear for all sufficient embedding dimensions, then one may have confidence in the extracted dimensionality of the phase space. In this work, estimates for α will be obtained directly from linear fits to the correlation sums.

Equations (5,6) pertain to the extraction of the correlation sums from one input time-series array: in that case, no database is available and the source of the embedding vectors must inevitably be the time-series array itself. The modification is straightforward if the division of the measurements into training and test sets is an option, as the case is in this work.

Let the database contain $M(m)$ embedding vectors $\tilde{\beta}_i$ for an embedding dimension m . Let also $N_k(m)$ be the number of embedding vectors, which can be constructed from the k -th test set, and N_t the number of files in the test set. The correlation sum for embedding dimension m would then be defined as

$$C(\epsilon) = \left(M(m) \sum_{k=1}^{N_t} N_k(m) \right)^{-1} \sum_{j=1}^{M(m)} \sum_{k=1}^{N_t} \sum_{i=1}^{N_k(m)} \Theta(\epsilon - \|\beta_{i,k} - \tilde{\beta}_j\|) , \quad (8)$$

where $\beta_{i,k}$ denotes the i -th embedding vector of the k -th test set.

To obtain reliable estimates for the correlation dimension, the $C(\epsilon)$ arrays were not processed if the triple sum in Eq. (8) yielded fewer than 10 (non-zero) contributions. The correlation sums were obtained at 40 ϵ values (i.e., between $4.50 \cdot 10^{-2}$ and $0.60 \cdot 10^{-2}$, with a step of $0.10 \cdot 10^{-2}$) and 10 embedding dimensions (i.e., $3 \leq m \leq 12$). The reason for choosing such a wide domain of embedding dimensions, in spite of having obtained m_0 in Section 5.4, is simple: this choice enables the study of the behaviour of the estimates for the dynamical invariants, e.g., for the correlation dimension and for the maximal Lyapunov exponent, in the transition from insufficient embedding dimensions to sufficient ones.

As explained earlier, one is interested in the domain of ϵ values for which the relationship between $\ln C(\epsilon)$ and $\ln \epsilon$ is linear; within this region,

$$\ln C(\epsilon) = \alpha \ln \epsilon + \beta \quad , \quad (9)$$

where the slope α is identified with $\alpha(N, \epsilon)$ of Eq. (7). At fixed m , the linearity between $\ln C(\epsilon)$ and $\ln \epsilon$ was investigated¹³, starting from the original $(\ln \epsilon, \ln C(\epsilon))$ points and removing the point with the largest ϵ value (one point per iteration), until the resulting p-value (obtained from the χ^2 value and the number of degrees of freedom in the linear fit) exceeded p_{\min} , the threshold of statistical significance (see Section 3). Table 5, and Figs. 5 and 6 contain the main results of the analysis of the correlation dimension for the problem dealt with in this paper.

The slope α of the linear fit of Eq. (9) should not be m -dependent for all sufficient embedding dimensions; this is the case for $10 \leq m \leq 12$. This result confirms the choice of 10 as the optimal embedding dimension in Section 5.4. Assuming only sufficient embeddings ($10 \leq m \leq 12$), one obtains for α the weighted average of 8.830 ± 0.062 .

5.6 Lyapunov exponents

I will next address the extraction of the maximal Lyapunov exponent from the measurements. Many regard the inability to reliably predict the future

¹³References [12] give the reader the impression that KS rather favour the visual inspection of the $(\ln \epsilon, \ln C(\epsilon))$ scatter plots as the means to establish the ϵ domain within which the linearity holds. My preference is to apply the appropriate statistical rules, and, if unable to perform an analysis as a result of the rigorousness of the conditions imposed, to rather relax these rigorous conditions in a consistent manner, e.g., by decreasing the threshold p_{\min} by one or two orders of magnitude.

Table 5

Results of the analysis of the correlation sums obtained using Eq. (8) for embedding dimensions between 3 and 12. The given domain $[\epsilon_{\min}, \epsilon_{\max}]$ corresponds to the ϵ domain within which the linearity between $\ln C(\epsilon)$ and $\ln \epsilon$ is accepted ($p \geq p_{\min}$).

m	ϵ_{\min}	ϵ_{\max}	α	$\delta\alpha$	β	$\delta\beta$
3	$6.00 \cdot 10^{-3}$	$1.80 \cdot 10^{-2}$	2.9573	0.0041	6.035	0.017
4	$6.00 \cdot 10^{-3}$	$1.80 \cdot 10^{-2}$	3.9156	0.0097	8.528	0.041
5	$6.00 \cdot 10^{-3}$	$1.80 \cdot 10^{-2}$	4.878	0.023	11.145	0.094
6	$6.00 \cdot 10^{-3}$	$1.90 \cdot 10^{-2}$	5.951	0.037	14.18	0.15
7	$8.00 \cdot 10^{-3}$	$1.90 \cdot 10^{-2}$	6.904	0.088	16.84	0.36
8	$1.10 \cdot 10^{-2}$	$2.40 \cdot 10^{-2}$	7.102	0.077	16.45	0.30
9	$1.40 \cdot 10^{-2}$	$2.50 \cdot 10^{-2}$	8.33	0.14	20.07	0.51
10	$1.60 \cdot 10^{-2}$	$2.80 \cdot 10^{-2}$	8.73	0.13	20.58	0.48
11	$1.80 \cdot 10^{-2}$	$3.20 \cdot 10^{-2}$	8.69	0.11	19.55	0.38
12	$1.90 \cdot 10^{-2}$	$3.90 \cdot 10^{-2}$	8.890	0.057	19.47	0.19

of chaotic systems, in spite of the known past and of a deterministic evolution, as the prominent characteristic of the chaotic behaviour. Of course, one needs to quantify what is meant by ‘reliably’ in the previous sentence. Predictions are routinely made in all systems, ordinary or chaotic (e.g., using autoregressive-moving-average (ARMA) models in linear analyses, Lorenz’s method of analogues in non-linear ones). The matter is that, in chaotic systems, neither do these predictions scatter around the observations (whenever they become available), nor does the difference between predicted and measured values increase linearly with time: the differences in chaotic systems (between predicted and measured values) grow exponentially with time (up to the time when the distance between the embedding vectors saturates). The Lyapunov exponents (usually denoted by λ) characterise the rapidity of the exponential divergence between predictions and observations (before the saturation effects prevail). In fact, one is predominantly interested in the maximal Lyapunov exponent (from now on, λ will stand for this exponent), as this quantity reflects the long-term behaviour of a chaotic system. The signature of deterministic chaos is a positive and finite λ value ($0 < \lambda < \infty$).

KS recommend one procedure for the determination of λ from a time-series array (of dimension N) and a database of embedding vectors (if no database is available, one may use the time-series array itself as the source of embedding vectors and predictions). The steps of this procedure may be summarised as follows.

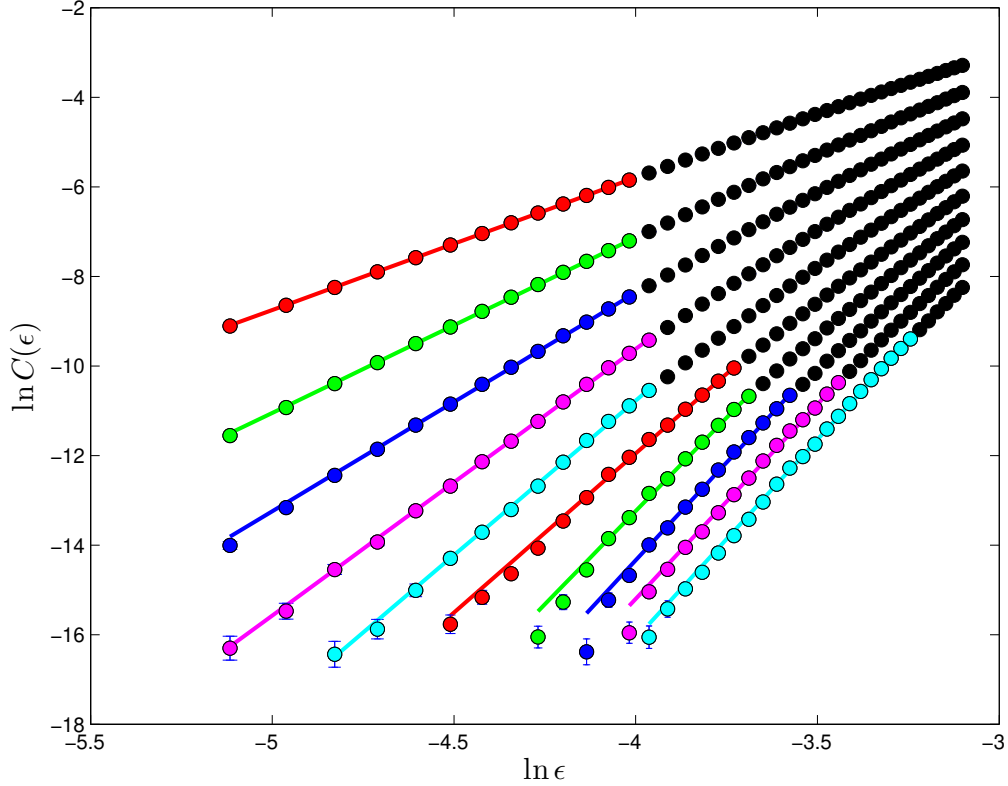


Fig. 5. The $(\ln \epsilon, \ln C(\epsilon))$ scatter plots for embedding dimensions $m = 3$ (top) to $m = 12$ (bottom). Weighted least-squares fits were performed on the data (see Table 5), separately for each embedding dimension in the ϵ domain within which the linearity between $\ln C(\epsilon)$ and $\ln \epsilon$ holds (coloured points and straight lines); the data outside these ϵ domains are also shown (in black). Although $\ln C(\epsilon)$ appears to depend linearly on $\ln \epsilon$ in broader ϵ domains, the rigorous test of linearity, based on the resulting χ^2 value and the number of degrees of freedom in each fit, fails for ϵ domains broader than those shown in this figure.

- Fix the embedding dimension m and the neighbourhood size ϵ .
- Commence with the element of the time-series array with index $i = 1 + (m - 1)\nu$ (the index of the first element of the time-series array is assumed to be 1).
- Construct the embedding vector β_i according to Eq. (2).
- Search the database for embedding vectors $\tilde{\beta}_j$, satisfying

$$d_{ij} := \|\beta_i - \tilde{\beta}_j\| \leq \epsilon . \quad (10)$$

Let the set of acceptable indices j (of the embedding vectors in the database, which neighbour the vector β_i in the context of Eq. (10)) be denoted as \mathcal{U}_i .

- Use the known futures in the original time series s (Δn sampling intervals after the i -th element) and in the database \tilde{s} (Δn sampling intervals after the

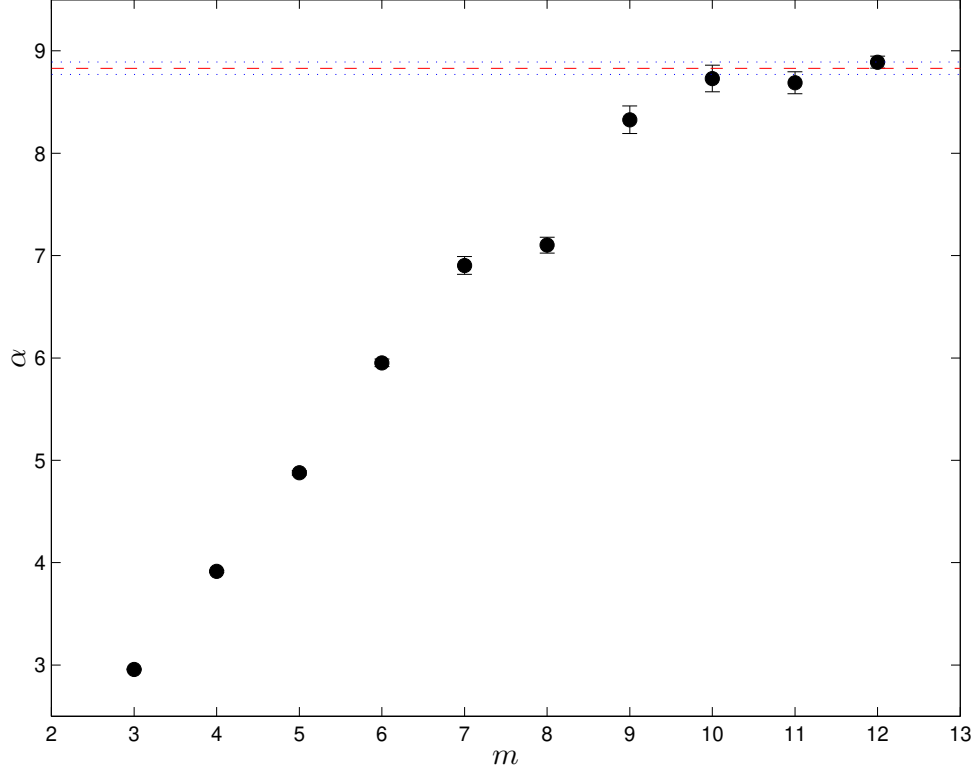


Fig. 6. The slope α of the linear fit to the correlation sum $\ln C(\epsilon)$, see Eq. (9). The red dashed line represents the weighted average over the α values for the sufficient embeddings ($10 \leq m \leq 12$), see Table 5. The blue dotted lines represent the 1σ limits of the statistical uncertainty, corrected for the quality of the reproduction of the three input α values by their weighted average.

last element of each embedding vector $\tilde{\beta}_j$) and store the absolute differences in an array:

$$Q_i(k) = \frac{1}{N_b} \sum_{j \in \mathcal{U}_i} |s_{i+k} - \tilde{s}_{j+k}| , \quad (11)$$

for $k \in \{0, 1, \dots, \Delta n\}$; N_b denotes the number of embedding vectors in \mathcal{U}_i .

- Obtain the natural logarithm of $Q_i(k)$ and the array of the average contributions over all index values i of the time-series array for which Δn predictions can be obtained:

$$S(k) = \frac{1}{N_c} \sum_{i=1+(m-1)\nu}^{N-\Delta n} \ln(Q_i(k)) , \quad (12)$$

where N_c denotes the number of elements in the original time series for which $\mathcal{U}_i \neq \emptyset$. The quantities $S(k)$ are known as out-of-sample prediction-error arrays. (Although KS suggest the use of N in Eq. (12), I believe that

the use of N_c is more convenient as it enables the direct comparison of the arrays obtained for different embedding dimensions.)

At this point, one remark is due. Technically, Eq. (12) is problematic from the strictly mathematical point of view: if, for some value of k , it so happens that $s_{i+k} = \tilde{s}_{j+k}$, $\forall j \in \mathcal{U}_i$, the logarithm is not defined. However, let me put aside such a possibility, anticipating that the ‘noise’ present in the time-series measurements precludes such critical situations.

I would like to suggest one modification to the method put forward by KS: Eq. (11) could be replaced by the form:

$$Q_i(k) = \left(\sum_{j \in \mathcal{U}_i} w_{ij} \right)^{-1} \sum_{j \in \mathcal{U}_i} w_{ij} |s_{i+k} - \tilde{s}_{j+k}|, \quad (13)$$

where the weights w_{ij} take account of the proximity of the embedding vectors β_i and $\tilde{\beta}_j$; the smaller the distance d_{ij} between these two vectors, the larger the weight of their contribution to the prediction-error array $Q_i(k)$. In this context, the method described in Refs. [12] would correspond to $w_{ij} \equiv 1$, whereas the results of this work have been obtained using $w_{ij} = 1 - (d_{ij}/\epsilon)^2$; I have no reason to expect sizeable systematic effects, but I believe that the statistical weights w_{ij} should be used. Obviously, the weight vanishes at $d_{ij} = \epsilon$ and, given the condition (10), it may be thought of as vanishing for $d_{ij} > \epsilon$. Of course, one may use higher (even) powers in the definition of the weights (perhaps, KS avoid the introduction of weights in the determination of $Q_i(k)$ due to this arbitrariness); the power of 4 was also used in this work, but the impact on the results was found insignificant.

In chaotic systems, $S(k)$ of Eq. (12) should be linearly increasing with k , up to the point where it saturates to the average absolute distance of two arbitrary embedding vectors on the attractor. KS emphasise the importance of the linearity of $S(k)$ (with k) at small k values; a positive slope seen on the $(k, S(k))$ scatter plot is indicative of chaotic behaviour.

Figure 7 shows all out-of-sample prediction-error arrays $S(k)$ corresponding to $\epsilon = 1.70 \cdot 10^{-2}$ (those not shown did not fulfil the acceptance criterion of the 10 non-zero contributions to $S(k)$). The plot is representative of the general behaviour of $S(k)$. The undulation of $S(k)$ is associated with the periodicity of the input data series. A linear segment in the $(k, S(k))$ scatter plot is rather difficult to find. On the other hand, it is evident that $S(k)$ increases with k (below about 40–50 sampling intervals) and saturates around 70 sampling intervals into the future. The outcome of the analysis of the luminosity measurements of PG 1159-035 resembles the one obtained by KS from far-infrared laser data (data sets SF_A and SF_Acont in Ref. [10]).

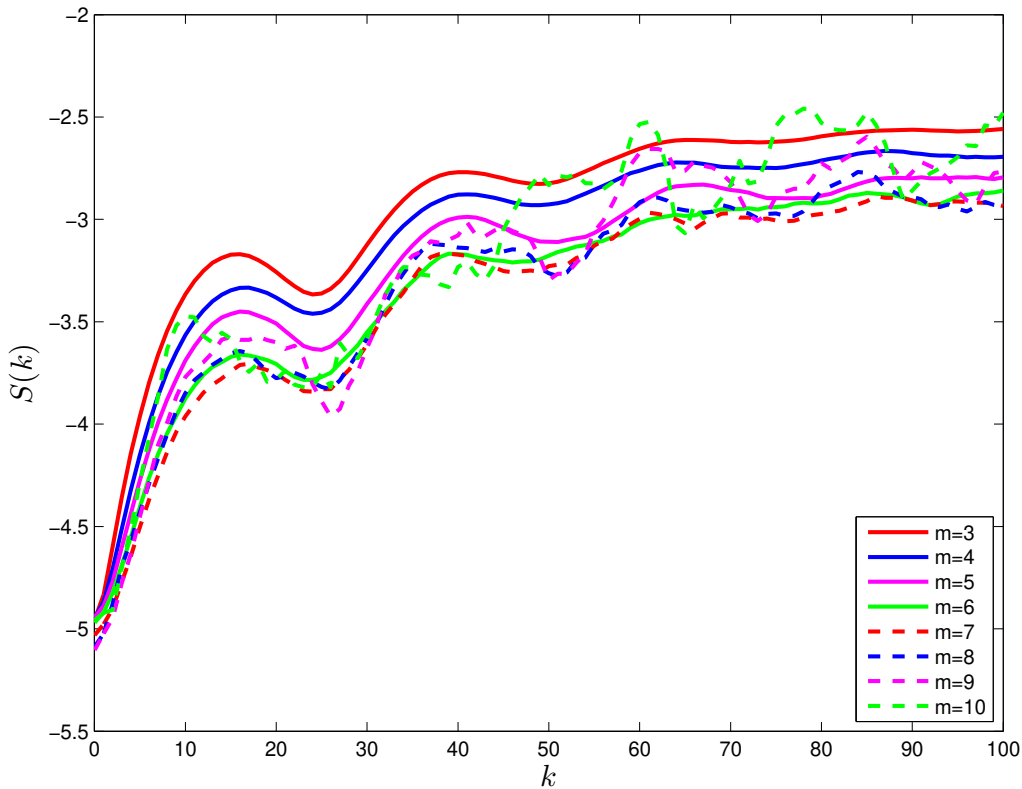


Fig. 7. The out-of-sample prediction-error arrays $S(k)$ (for the details, see Section 5.6) corresponding to the neighbourhood size $\epsilon = 1.70 \cdot 10^{-2}$.

One way to cope with the undulations of $S(k)$ would be to analyse the local extrema and derive limits for the maximal Lyapunov exponent; however, such an analysis would rest upon very few data points. A better option is to fit a suitable monotonic function to the $S(k)$ values and capture the general trend of $S(k)$; this option will be followed in the remaining part of this section.

For the purpose of fitting to the $S(k)$ arrays, the MINUIT package [21] of the CERN library (FORTRAN version) was used. Each optimisation was achieved with the (robust) sequence: SIMPLEX, MINIMIZE, MIGRAD, and MINOS.

- SIMPLEX is a function-minimisation method, using the simplex method of Nelder and Mead. Being a stepping method, SIMPLEX does not produce a Hessian matrix.
- MINIMIZE minimises the user-defined function by calling MIGRAD and reverts to SIMPLEX in case that the MIGRAD call fails to converge.
- MIGRAD is the workhorse of the MINUIT software library. It is a variable-metric method, also checking for the positive-definiteness of the Hessian matrix.

- MINOS performs a detailed error analysis for each of the model parameters separately. It may be time consuming, but its results (i.e., the asymmetric uncertainties of the model parameters) are reliable as they take the non-linearities into account, as well as the correlations among the model parameters.

All the aforementioned methods admit an optional argument, limiting the maximal number of calls of the method; if this number is reached, that method is terminated (by MINUIT, internally) regardless of whether it has converged or not. To ensure the successful termination of the MINUIT application and the convergence of its methods, the output of the application was automatically displayed and checked for failures.

The original out-of-sample prediction-error arrays $S(k)$, obtained by the appropriate variation of the quantities m and ϵ (i.e., within the linearity region in the $(\ln \epsilon, \ln C(\epsilon))$ scatter plots), were fitted to by the function

$$S(k) = \ln \left[x_1 \exp \left[x_2 \left(1 + \frac{x_3}{x_1} \right) k \right] + x_3 \right] , \quad (14)$$

where the parameters $x_{1,2,3}$ are associated with the variation of $S(k)$ between $k = 0$ and saturation, the maximal Lyapunov exponent (λ), and the saturation level of $S(k)$, respectively; the expansion of $S(k)$ of Eq. (14) for small k values is: $S(k) \approx \ln(x_1 + x_3) + x_2 k$. Other suitable three-parameter forms were also tried, but generally gave inferior χ^2 results. Nevertheless, results were also obtained (for the sake of comparison) with one of these alternative forms, namely

$$S(k) = x_3 - \frac{x_2 x_1^2}{k - x_1} , \quad (15)$$

where the meaning of the parameters x_2 and x_3 is the same as for the form (14), whereas $x_1 < 0$ in the case of the form (15) represents the position of the vertical asymptote of the hyperbolic form; the expansion of $S(k)$ of Eq. (15) for small k values is: $S(k) \approx x_3 + x_1 x_2 + x_2 k$.

A constant working uncertainty of 0.1 was assigned to each input value. Given the redefinition of the fitted uncertainties, taking account of the quality of each fit via the application of the Birge factor $\sqrt{\chi^2/\text{NDF}}$ (NDF stands for the number of degrees of freedom in the fit, namely the number of input data points reduced by the number of the fit parameters, i.e., 3), the value of the assigned uncertainty is irrelevant, i.e., the choice of another (non-zero) value leads to identical results. The optimisation application did not terminate successfully in 4 (out of 140) cases, which (of course) had to be excluded. (No failures were found when the data were fitted to by the form of Eq. (15).) The results of a representative fit (original and fitted $S(k)$ data) are shown in Fig. 8.

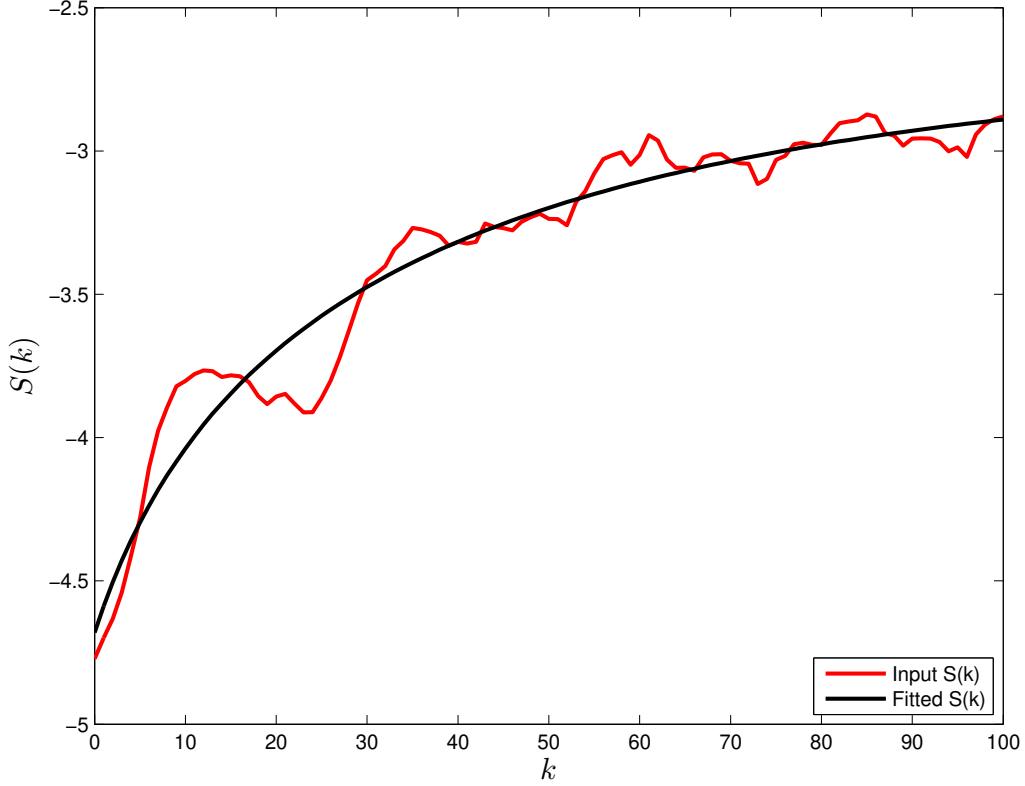


Fig. 8. Original and fitted values of an out-of-sample prediction-error array $S(k)$, see Eq. (12). The figure corresponds to $m = 10$ and $\epsilon = 2.10 \cdot 10^{-2}$, which yields a χ^2 value close to the median value obtained in the original fits to the $S(k)$ arrays.

To obtain reliable estimates for λ , the results of the fits were processed further. The minimal value of χ^2 , obtained from these fits, was equal to 46.02 (for 97 degrees of freedom), whereas the maximal one was 1539.73. Inspection of the χ^2 histogram demonstrated that, though reasonable values were obtained in most cases, unreasonably large χ^2 results were generally obtained when the acceptance criterion of the 10 non-zero contributions to $S(k)$ was barely fulfilled. The average χ^2 was equal to about 187.53, whereas the median value was 120.90. To be rid of the cases with unreasonably large χ^2 values, an acceptance criterion was introduced, at twice the median χ^2 value of the original distribution. As a result, fits were accepted only if $\chi^2 \lesssim 241.80$. Discarded were 22 (out of the original 136) fits; the remaining cases were processed further, yielding the main results of this work.

The maximal Lyapunov exponents extracted from the filtered luminosity measurements of PG 1159-035 for $3 \leq m \leq 12$ are shown in Fig. 9. Noticeable in this figure is the decrease of the uncertainties with increasing embedding dimension; this is the result of the better compatibility of the ex-

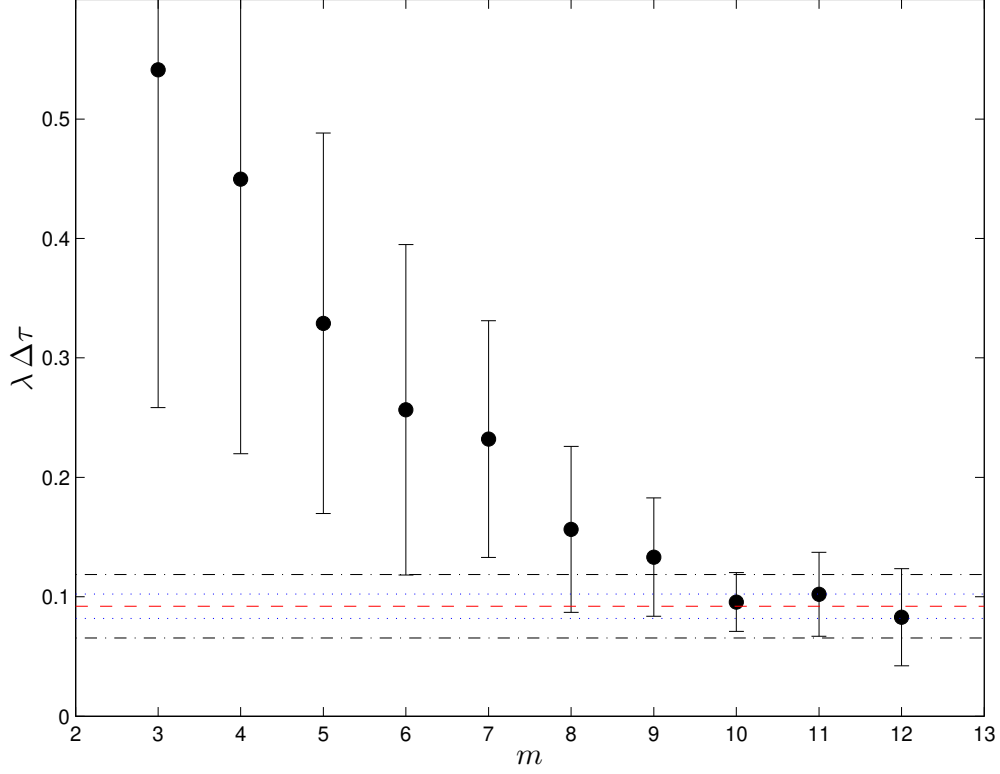


Fig. 9. The maximal Lyapunov exponents extracted from the filtered luminosity measurements of PG 1159-035 using Eq. (14). The sum of the statistical and systematic uncertainties is shown for each data point; the statistical uncertainties have been corrected for the quality of each fit. The red dashed line represents the grand mean over the ϵ values for the sufficient embeddings ($10 \leq m \leq 12$). The blue dotted lines represent the 1σ limits of the statistical uncertainty of the grand mean, whereas the black dash-dotted lines correspond to the (1σ limits of the) systematic uncertainty.

tracted λ values for the different neighbourhood sizes as the embedding dimension approaches the optimal one. The values should be compatible for all sufficient embeddings, and indeed they are. One conclusion may be drawn from this plot: the maximal Lyapunov exponent is positive. Restricting the analysis only to sufficient embeddings ($10 \leq m \leq 12$), one obtains $\lambda = (9.2 \pm 1.0(\text{stat.}) \pm 2.7(\text{syst.})) \cdot 10^{-2} \Delta\tau^{-1}$. The first uncertainty is statistical (average over fitted uncertainties, corrected for the quality of each fit), the second systematic (reflecting the variation of λ with ϵ for the sufficient embeddings). (The use of the hyperbolic form of Eq. (15) in the fits yielded a compatible result, namely $\lambda = (8.3 \pm 1.0(\text{stat.}) \pm 2.3(\text{syst.})) \cdot 10^{-2} \Delta\tau^{-1}$.)

Table 6

The equivalent of Table 5 when the L^2 -norm distance is used in the determination of the correlation sums.

m	ϵ_{\min}	ϵ_{\max}	α	$\delta\alpha$	β	$\delta\beta$
3	$6.00 \cdot 10^{-3}$	$2.10 \cdot 10^{-2}$	2.9683	0.0035	5.445	0.014
4	$6.00 \cdot 10^{-3}$	$2.50 \cdot 10^{-2}$	3.9191	0.0071	7.398	0.028
5	$6.00 \cdot 10^{-3}$	$2.70 \cdot 10^{-2}$	4.884	0.016	9.430	0.059
6	$9.00 \cdot 10^{-3}$	$3.00 \cdot 10^{-2}$	5.978	0.029	11.82	0.11
7	$1.30 \cdot 10^{-2}$	$3.20 \cdot 10^{-2}$	7.021	0.056	14.03	0.20
8	$1.90 \cdot 10^{-2}$	$3.70 \cdot 10^{-2}$	7.848	0.081	15.40	0.27
9	$2.50 \cdot 10^{-2}$	$3.90 \cdot 10^{-2}$	9.99	0.21	20.99	0.68
10	$2.90 \cdot 10^{-2}$	$4.30 \cdot 10^{-2}$	11.04	0.25	22.88	0.81
11	$3.40 \cdot 10^{-2}$	$4.50 \cdot 10^{-2}$	11.41	0.33	22.7	1.0
12	$3.80 \cdot 10^{-2}$	$4.50 \cdot 10^{-2}$	12.80	0.37	25.7	1.2

5.7 Changes in the important results when the L^2 -norm distance is used

The results of Sections 5.5 and 5.6, obtained with the use of the L^∞ distance, are the main results of this work. Assessed in this section is the importance of the changes when using a different norm in the quantification of the closeness of two embedding vectors, namely the L^2 norm (Euclidean distance). At fixed ϵ , the change from the L^∞ to the L^2 distance leads to the extraction of a smaller number of neighbours, hence contributions to the correlation sums and to the out-of-sample prediction-error arrays $S(k)$. Therefore, the increase of the uncertainty of the extracted estimates for the maximal Lyapunov exponent is expected.

The linearity between $\ln C(\epsilon)$ and $\ln \epsilon$ was investigated as in Section 5.5. As in the case of the L^∞ distance, the out-of-sample prediction-error arrays $S(k)$ were created and further analysed only if at least 10 neighbours could be found in the database. Table 6 is the equivalent of Table 5 in the case of the L^2 -norm distance. One notices that the slope α does not saturate with increasing embedding dimension; at the present time, I cannot explain why.

The out-of-sample prediction-error arrays $S(k)$ were obtained and fitted to, as described in Section 5.6. The maximal Lyapunov exponent was extracted using Eq. (14) for all embedding dimensions and $\epsilon_{\min} \leq \epsilon \leq \epsilon_{\max}$ (linearity region in the $(\ln \epsilon, \ln C(\epsilon))$ plane, see Table 6). An upper cut was applied to

the resulting χ^2 values as in Section 5.6. The final outcome is: $\lambda = (16.4 \pm 2.0(\text{stat.}) \pm 5.0(\text{syst.})) \cdot 10^{-2} \Delta\tau^{-1}$, larger than, yet not incompatible with, the more accurate result obtained with the L^∞ distance.

6 Discussion and conclusions

The goal of this work was the analysis of the luminosity measurements of the pre-white dwarf PG 1159-035, in fact those of the measurements which found their way to the ‘Time-series data source Archives: Santa Fé Time Series Competition’ [10]. It is my belief that the set of the experimental data, acquired in the 1989 runs of the Whole Earth Telescope (WET) project, is considerably more extensive.

Following the results of Refs. [2,3], the seventeen available time series were suitably band-passed using an elliptical filter, whose 13 recursion coefficients are listed in Table 3. The filtered data was split into two parts of comparable sizes, one yielding the training (learning) set or database, the second the test set. The optimal embedding dimension was determined using Cao’s method [18], see Section 5.4: it appears that optimal embeddings require a 10-dimensional space. This choice was confirmed in Section 5.5 by an analysis of the correlation dimension.

The extraction of the maximal Lyapunov exponent λ was next attempted by fitting a monotonic function (see Eq. (14)) to the out-of-sample prediction-error arrays $S(k)$, defined in Eq. (12); the original arrays contain sizeable undulations, hindering the determination of a region in the $(k, S(k))$ plane within which a linear relationship (i.e., the signature of a chaotic dynamical system) holds. A modification is proposed in this work in the evaluation of the $S(k)$ arrays, taking account of the distance between the specific embedding vector of the test set and its corresponding partner in the training set: the smaller the distance between these two vectors, the larger the weight assigned to the associated predictions in the determination of the out-of-sample prediction-error arrays $S(k)$, see Eq. (13).

The data analysis suggests that the maximal Lyapunov exponent λ , associated with the luminosity measurements of PG 1159-035, is equal to $(9.2 \pm 1.0(\text{stat.}) \pm 2.7(\text{syst.})) \cdot 10^{-2} \Delta\tau^{-1}$, where $\Delta\tau$ represents the sampling interval in the measurements (10 s). It was found that the extracted λ values do not show significant dependence on the embedding dimension for sufficient embeddings ($10 \leq m \leq 12$), see Fig. 9. The findings of this work suggest that it is very likely that the source of the observations is indeed chaotic.

The aforementioned results refer to the use of the L^∞ -norm distance. Inter-

estingly, the use of the Euclidean (L^2 -norm) distance yields a larger, yet not incompatible, result for the maximal Lyapunov exponent.

This work is the first step I have taken in analysing the luminosity measurements of the pre-white dwarf PG 1159-035. I would be glad to receive the entirety of the data (1989 runs) from a credible source, e.g., directly from one of the members of the WET Collaboration. The analysis of the data after suitably involving all files in both the training and the test sets is currently under investigation [22].

Acknowledgements

I acknowledge an e-mail exchange with S. Hollos.

All the figures have been created with MATLAB [®] (The MathWorks, Inc., Natick, Massachusetts, United States).

References

- [1] R.F. Green, M. Schmidt, J. Liebert, ‘The Palomar-Green catalog of ultraviolet-excess stellar objects’, *Astrophys. J. Suppl. S.* 61 (1986) 305–352. DOI: 10.1086/191115
- [2] D.E. Winget et al., ‘Asteroseismology of the DOV star PG 1159-035 with the Whole Earth Telectope’, *Astrophys. J.* 378 (1991) 326–346. DOI: 10.1086/170434
- [3] J.E.S. Costa et al., ‘The pulsation modes of the pre-white dwarf PG 1159-035’, *Astron. Astrophys.* 477 (2008) 627–640. DOI: 10.1051/0004-6361:20053470
- [4] S.D. Kawaler, P.A. Bradley, ‘Precision Asteroseismology of pulsating PG 1159 stars’, *Astrophys. J.* 427 (1994) 415–428. DOI: 10.1086/174152
- [5] E. García-Berro et al., ‘The gravitational wave radiation of pulsating white dwarfs revisited: the case of BPM 37093 and PG 1159-035’, *Astron. Astrophys.* 446 (2006) 259–266. DOI: 10.1051/0004-6361:20053781
- [6] A.H. Córscico, L.G. Althaus, ‘Asteroseismic inferences on GW Virginis variable stars in the frame of new PG 1159 evolutionary models’, *Astron. Astrophys.* 454 (2006) 863–881. DOI: 10.1051/0004-6361:20054199
- [7] A.H. Córscico, L.G. Althaus, S.O. Kepler, J.E.S. Costa, M.M. Miller Bertolami, ‘Asteroseismological measurements on PG 1159-035, the prototype of the GW Virginis variable stars’, *Astron. Astrophys.* 478 (2008) 869–881. DOI: 10.1051/0004-6361:20078646

- [8] L.G. Althaus, A.H. Córscico, M.M. Miller Bertolami, E. García-Berro, S.O. Kepler, ‘Evidence of thin helium envelopes in PG 1159 stars’, *Astrophys. J. Lett.* 677 (2008) L35–L38. DOI: 10.1086/587739
- [9] J.E.S. Costa, S.O. Kepler, ‘The temporal changes of the pulsational periods of the pre-white dwarf PG 1159-035’, *Astron. Astrophys.* 489 (2008) 1225–1232. DOI: 10.1051/0004-6361:20079118
- [10] <http://www.comp-engine.org>
- [11] R. Hegger, H. Kantz, T. Schreiber, ‘TISEAN 3.0.1, Nonlinear Time Series Analysis’, https://www.pks.mpg.de/~tisean/Tisean_3.0.1/index.html
- [12] H. Kantz, T. Schreiber, ‘Nonlinear Time Series Analysis’, Cambridge University Press, 1997; 2nd Edn., Cambridge University Press, 2004. ISBN: 0521821509, 0521529026
- [13] B. Rosner, ‘Percentage points for a generalized ESD many-outlier procedure’, *Technometrics* 25 (1983) 165–172. DOI: 10.2307/1268549
- [14] F.E. Grubbs, ‘Procedures for detecting outlying observations in samples’, *Technometrics* 11 (1969) 1–21. DOI: 10.2307/1266761
- [15] W. Stefansky, ‘Rejecting outliers in factorial designs’, *Technometrics* 14 (1972) 469–479. DOI: 10.2307/1267436
- [16] F. Takens, ‘Detecting strange attractors in turbulence’, pp. 366-381 in ‘Dynamical Systems and Turbulence (Lecture Notes in Mathematics)’, Springer-Verlag, 1981. ISBN: 0387111719
- [17] P. Grassberger, I. Procaccia, ‘Measuring the strangeness of strange attractors’, *Physica D* 9 (1983) 189–208. DOI: 10.1016/0167-2789(83)90298-1
- [18] L. Cao, ‘Practical method for determining the minimum embedding dimension of a scalar time series’, *Physica D* 110 (1997) 43–50. DOI: 10.1016/S0167-2789(97)00118-8
- [19] M.B. Kennel, R. Brown, H.D.I. Abarbanel, ‘Determining embedding dimension for phase-space reconstruction using a geometrical construction’, *Phys. Rev. A* 45 (1992) 3403–3411. DOI: 10.1103/PhysRevA.45.3403
- [20] A. Krakovská, K. Mezeiová, H. Budáčová, ‘Use of False Nearest Neighbours for selecting variables and embedding parameters for state space reconstruction’, *J. Complex Syst.* 2015 (2015) 932750. DOI: 10.1155/2015/932750
- [21] F. James, ‘MINUIT - Function Minimization and Error Analysis’, CERN Program Library Long Writeup D506.
- [22] E. Matsinos, ‘Analysis of luminosity measurements of the pre-white dwarf PG 1159-035: an approach featuring a dynamical database’, in preparation.